Average Rician K-Factor Based Analytical Uncertainty Model for Total Radiated Power Measurement in a Reverberation Chamber

TIANYUAN JIA[1], **YI HUANG**[1], **(Senior Member, IEEE), QIAN XU**[2], **(Member, IEEE),**
QIANG HUA[1]**, AND LYUWEI CHEN**[1]

[1]Department of Electrical Engineering and Electronics, University of Liverpool, Liverpool L69 3GJ, U.K.
[2]College of Electronics and Information Engineering, Nanjing University of Aeronautics and Astronautics, Nanjing 211106, China

Corresponding author: Yi Huang (yi.huang@liverpool.ac.uk)

ABSTRACT Total radiated power (TRP) is commonly accepted as an important figure of merit (FoM) for evaluating the over-the-air (OTA) performance of wireless devices enabled by the emerging fifth generation (5G) mobile communication technology. The statistically homogeneous and isotropic electromagnetic (EM) environment created by a reverberation chamber (RC) makes it an accurate, efficient, and economic testing facility for TRP measurement. In this paper, an improved analytical uncertainty model which is based on the average Rician K-factor (K_{avg}) and the number of independent samples is proposed for TRP measurement using an RC. It has the flexibility to allow different stirring configurations in the calibration stage and the measurement stage, and gives insight into the measurement uncertainty without the tedious and inefficient empirical estimation processes. Estimators of K_{avg} are modelled and analyzed. Specifically, the maximum likelihood estimator (MLE) of K_{avg} is validated by the Monte Carlo simulation, and its unbiased correction is derived accordingly for improved uncertainty model accuracy. Extensive 9-Point estimation measurements are also conducted in order to evaluate the performance of the proposed analytical model.

INDEX TERMS Average Rician K-factor, fifth generation (5G), independent sample number, measurement uncertainty, over-the-air (OTA) testing, reverberation chamber (RC), statistical analysis, total radiated power (TRP).

I. INTRODUCTION

While continuously reshaping our way of life, the emerging fifth generation (5G) wireless technologies [1], [2] also introduce various challenges to the instrumentation and measurement society [3]–[5]. Massive multi-input multi-output (MIMO) composes a large number of antenna elements, which focus the radiated energy towards the desired directions of propagation, and serve multiple users simultaneously using the full frequency spectrum resources. However, due to its high integration, single antenna port in a typical massive MIMO system is no longer accessible as different from the traditional MIMO system. Besides, the use of adaptive antenna technologies for 5G enabled devices makes its system level performance largely differ from the simple combination of the conducted testing results for individual

components. Consequently, the paradigm shift in terms of testing methodology from conducted to over-the-air (OTA) is necessary.

Total radiated power (TRP) has been widely adopted as a figure of merit (FoM) by standardization organizations for 5G OTA conformance testing. Non-directional requirements including but not restricted to output power, adjacent channel leakage ratio (ACLR), operating band unwanted emissions (OBUE), spectrum emission mask (SEM) and spurious can be characterized and quantified via TRP measurements.

Reverberation chambers (RC) [6]–[8] are essentially electrically large shielded enclosures with high quality factor (Q) values. By utilizing multiple stirring techniques [9]–[14] to alter the boundary conditions, statistically homogeneous and isotropic electromagnetic (EM) field environment can be achieved within the working volume of the RC. Owing to this unique property, RC-based measurement of non-directional

The associate editor coordinating the review of this manuscript and approving it for publication was Xiaoming Chen.

parameters including TRP can be efficient and accurate. Originally, it was primarily used in the electromagnetic compatibility (EMC) realm like radiated emission and radiated immunity tests [15]. Recently, the RC has become a promising candidate facility for OTA testing of wireless devices, and the relevant techniques are continuously evolving with the new testing requirements of 5G. Up to now, the RC has already been standardized for OTA TRP measurements of user equipment (UE) [16] and large-form-factor machine-to-machine (M2M) devices [17], and discussion about the standardization process is ongoing in terms of the base station (BS) testing [18].

In order to thoroughly evaluate the performance of a testing technique, it is of crucial importance to quantify its measurement uncertainty. Since an RC is typically modelled and employed as a stochastic process, the measurement uncertainty analysis should stem from its statistical characteristics. So far, Numerous studies have been conducted in this field [9], [11], [13], [14], [19]–[27]. It is commonly accepted that for a practical RC that inevitably renders non-zero unstirred power, the corresponding measurement uncertainty dependents not only on the finite number of independent samples [9], [19], but also on the limited spatial uniformity [11], [20]–[26]. Sometimes, the latter can even dominate the uncertainty [21].

The Rician K-factor (K) [28]–[31], which is defined as the ratio of the unstirred power to the stirrer power, is a suitable measure of this nonuniformity effect. Therefore, uncertainty formulations proposed by various researchers [11], [20]–[22] adopt the explicit representation of K for improved model performance. However, there are several concerns when using K in uncertainty models: a) K has its own measurement uncertainty; b) when applying source stirring (like rotating platform stirring and polarization stirring) and frequency stirring, the value of K actually varies; c) it is hard, if not impossible, to acquire the value of K when measuring the device under test (DUT); d) the reference measurement of a single-case K might be quite different from that for the DUT measurement. As a result, the average Rician K-factor (K_{avg}), which is based on the assumption of random unstirred power [11], [32], [33], should be used instead. K_{avg} was first adopted by [11], but the corresponding uncertainty model was derived heuristically by empirical assumptions. The analytical expression in [20] was based on the components-of-variance model, and K appeared in the expression is equivalent to K_{avg} when source stirring is conducted. However, there was no analysis about how to estimate K_{avg} and the corresponding uncertainty. Reference [22] simply pooled multiple single-case K values, which is mathematically viable but lacks physical meaning.

Furthermore, to date a pure analytical uncertainty model for the TRP measurement using an RC reflecting the impacts of both stages (*i.e.* the calibration stage and the measurement stage) as well as the spatial uniformity is still unavailable in literature.

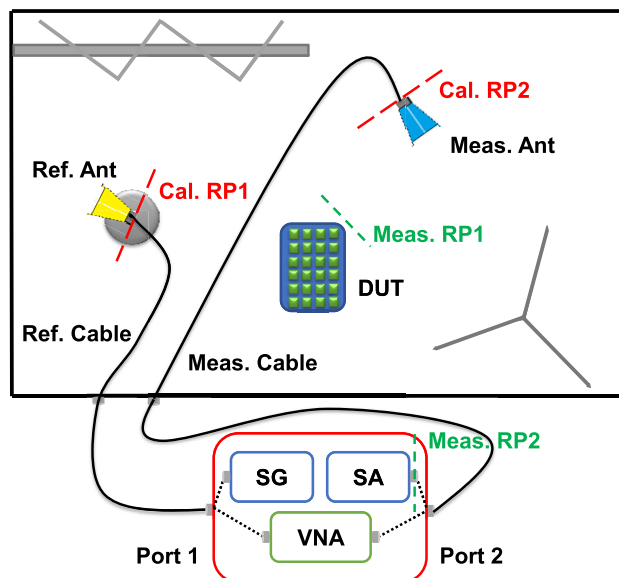Contributions of this work are summarized as follows:

FIGURE 1. Schematic diagram of typical RC based TRP measurement setup. The dotted lines represent virtual connections so that the vector network analyzer (VNA) or signal generator (SG)/signal analyzer (SA) can be chosen on demand; the two dashed line pairs indicate the positions of the reference planes (RPs) for the relevant stages.

1) K_{avg} is formulated based on the random unstirred power assumption, and statistical models for different estimators of K_{avg} are obtained (Section II).
2) The maximum likelihood estimator (MLE) of K_{avg} is verified by Monte Carlo simulations, and the corresponding unbiased estimator is given (Section II).
3) An analytical relative uncertainty model based on independent sample numbers and K_{avg} considering both stages for the TRP measurement is derived. It allows different stirring configurations in each stage, and makes it possible to characterize the measurement dispersion without tedious and inefficient empirical estimation processes (Section III).
4) Extensive measurements are performed using the 9-Point estimation procedure to validate the proposed analytical model (Section IV).

II. K_{avg}: FORMULATION AND STATISTICAL MODELLING OF RELEVANT ESTIMATORS

A. FORMULATION OF K_{avg}

Without loss of generality, the samples provided by each stirring technique are considered as independent in this section. Sample correlation and derivation of independent sample numbers for different stirring techniques will be discussed in detail in Section IV. A typical RC-based measurement setup is depicted in Fig. 1. Assume that a complete mechanical stirring process generates N samples [9], and the same process is repeated $L = M \cdot F$ times at M source positions [10], [11] and F frequency points [12]–[14] for further decreasing the measurement uncertainty. Here, for frequencies separated larger than the coherent bandwidth (so that they can be considered

as independent), the corresponding spatial channels experienced are quite different according to the propagation theory. For each stirrer sequence l, the complex-valued transmission coefficient $S_{21}(l)$ measured by a vector network analyzer (VNA) can be modeled as the superposition of two terms [11]:

$$S_{21}(l) = S_{21,s}(l) + S_{21,us}(l) \tag{1}$$

$S_{21,s}(l)$ is the stirred component of $S_{21}(l)$ that is fully interacted with the mechanical stirrers of the RC. It follows a complex circular Gaussian distribution with zero-mean and variance σ_s^2 [6]:

$$S_{21,s}(l) = S_{21,s}^{re}(l) + jS_{21,s}^{im}(l) \sim \mathcal{N}\left(0, \sigma_s^2\right) + j\mathcal{N}\left(0, \sigma_s^2\right) \tag{2}$$

where the superscripts *re* and *im* are the real and imaginary parts, respectively, and they are independent and identically distributed (i.i.d.).

$S_{21,us}(l)$, the unstirred component, is the residual that remains unaffected during the stirrer rotating, which is assumed to be a deterministic complex value:

$$S_{21,us}(l) = S_{21,us}^{re}(l) + jS_{21,us}^{im}(l) = \mu_{re}(l) + j\mu_{im}(l) \tag{3}$$

where $\mu_{re}(l)$ and $\mu_{im}(l)$ are two unknown constants (but dependent upon l). In practice, the above two components are estimated by the following estimators:

$$\hat{S}_{21,us}(l) = \langle S_{21}(l)\rangle_N = \langle S_{21}^{re}(l)\rangle_N + j\langle S_{21}^{im}(l)\rangle_N$$
$$= \hat{\mu}_{re}(l) + j\hat{\mu}_{im}(l) \tag{4}$$

$$\hat{S}_{21,s}(l) = S_{21}(l) - \langle S_{21}(l)\rangle_N$$
$$= \left(S_{21}^{re}(l) - \hat{\mu}_{re}(l)\right) + j\left(S_{21}^{im}(l) - \hat{\mu}_{im}(l)\right) \tag{5}$$

where $<>$ denotes the ensemble average operation, and $\hat{}$ is the estimator symbol of the relevant quantity.

For the l_{th} mechanical stirring process, the single-case Rician *K*-factor is defined as follows [28]

$$K(l) = \frac{P_{us}(l)}{P_{s,avg}(l)} = \frac{P_{us}(l)}{E[P_s(l)]} \tag{6}$$

where

$$P_{us}(l) = |S_{21,us}(l)|^2 = \mu_{re}^2(l) + \mu_{im}^2(l) \tag{7}$$

is the unstirred power, and

$$P_s(l) = |S_{21,s}(l)|^2 \sim Exp(1/2\sigma_s^2) \tag{8}$$

is the stirred power which follows an exponential distribution with mean (also standard deviation)

$$P_{s,avg}(l) = E[P_s(l)] = 2\sigma_s^2 \tag{9}$$

Based on (4) and (5), the maximum likelihood (MLE) estimators of (7) and (9) are given as:

$$\hat{P}_{us}(l) = \left|\hat{S}_{21,us}(l)\right|^2 = \hat{\mu}_{re}^2(l) + \hat{\mu}_{im}^2(l) \tag{10}$$

$$\hat{P}_{s,avg}(l) = \frac{1}{N-1}\sum_{n=1}^{N}\left|\hat{S}_{21,s}(l)\right|^2$$

$$= \frac{1}{N-1}\sum_{n=1}^{N}\left|S_{21}^{re}(l) - \hat{\mu}_{re}(l)\right|^2$$
$$+ \frac{1}{N-1}\sum_{n=1}^{N}\left|S_{21}^{im}(l) - \hat{\mu}_{im}(l)\right|^2 \tag{11}$$

Detailed statistical modelling of different estimators of $K(l)$ can be found in [29]–[31].

Furthermore, when all the L realizations are considered simultaneously (so that the dependency of l can be suppressed), the resultant unstirred part cannot be regarded as a constant anymore. If L is large enough so that the ergodic condition is fulfilled, it should be described as a stochastic process [11], [32]. According to [20], the random unstirred component $S_{21,us}$ is modeled by a complex circular Gaussian distribution with zero-mean and variance σ_{us}^2:

$$S_{21,us} = S_{21,us}^{re} + jS_{21,us}^{im} = \mu_{re} + j\mu_{im}$$
$$\sim \mathcal{N}\left(0, \sigma_{us}^2\right) + j\mathcal{N}\left(0, \sigma_{us}^2\right) \tag{12}$$

Compared with (3), it is now clear that $\mu_*(l)$ (and thus $S_{21,us}(l)$) is essentially a sample drawn from the corresponding random distribution $\mu_*(S_{21,us})$ in (12). Conversely, as already implied in (2) and (8), the statistical characteristics of the stirred part remains intact throughout the L realizations (*i.e.*, independent of l).

From the above analysis, the average Rician *K*-factor can be formulated as follows [33]:

$$K_{avg} = \frac{P_{us,avg}}{P_{s,avg}} = \frac{E[P_{us}]}{E[P_{s,avg}(l)]} \tag{13}$$

where

$$P_{us} = |S_{21,us}|^2 = |\mu_{re}|^2 + |\mu_{im}|^2 \sim Exp(1/2\sigma_{us}^2) \tag{14}$$

is the random unstirred power which follows an exponential distribution with mean (also standard deviation)

$$P_{us,avg} = E[P_{us}] = 2\sigma_{us}^2 \tag{15}$$

Similarly, $P_{us}(l) = \mu_{re}^2(l) + \mu_{im}^2(l)$ in (7) is the l_{th} sample drawn from the distribution in (14). With the purpose of verifying the theoretical distribution of P_{us}, 1601 frequency points (in the frequency range 3.4 GHz – 3.6 GHz) are collected as samples and the corresponding measured cumulative distribution function (CDF) is plotted and compared with the theoretical exponential CDF (as shown in Fig. 2). Not surprisingly, good agreement is achieved between theory (dashed) and experimental result (solid). This also proves that frequency stirring can provide randomness to the unstirred non-line-of-sight (NLOS) component.

As for the denominator part of (13), regarding (9),

$$P_{s,avg} = E[P_{s,avg}(l)] = E[E[P_s(l)]] = 2\sigma_s^2 \tag{16}$$

Substituting (15) and (16) into (13) gives
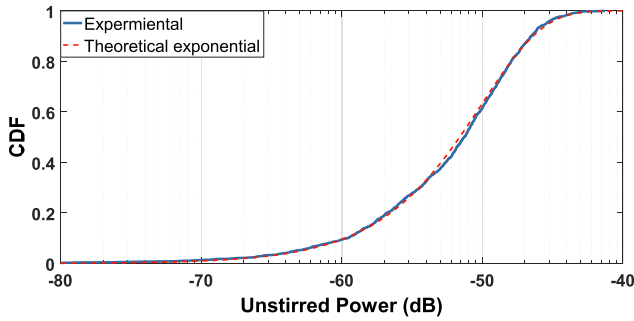
$$K_{avg} = \frac{\sigma_{us}^2}{\sigma_s^2} \tag{17}$$

FIGURE 2. Comparisons of the theoretical and experimental CDF of P_{us} using adjacent frequency points (3.4 GHz – 3.6 GHz) as samples.

FIGURE 3. Comparisons of the theoretical and experimental CDF of (a) $\langle P_s(l) \rangle_N$ using adjacent frequency points (3.475 GHz – 3.525 GHz) as samples. (b) $\langle P_s(l) \rangle_L$ using different stirrer positions as samples. In both subplots, the black dash-dot curve is with the optimal shape parameter value, while the red dashed curve is with an arbitrary suboptimal shape parameter value for comparison.

which is the ground truth value. It can be seen that (13) is a necessary continuation of (6) in order to characterize an RC when multiple stirring techniques are utilized.

B. ESTIMATOR OF K_{avg} WHEN SAMPLES OF $S_{21,s}(l)$ AND $S_{21,us}$ CAN BE DRAWN INDEPENDENTLY

Assume that samples of $S_{21,s}(l)$ and $S_{21,us}$ can be drawn independently from the unknown distributions (2) and (12). Taking into consideration that the number of available samples (both N and L) are finite, a basic estimator of (13) is given as:

$$\hat{K}_{avg} = \frac{V}{U} = \frac{\langle P_{us} \rangle_L}{\langle P_s(l) \rangle_{N,L}} \quad (18)$$

the use of U and V are for notational convenience. Based on (8), U follows a Gamma distribution

$$U \sim Gamma\left(NL, NL/2\sigma_s^2\right) \quad (19)$$

with $E[U] = 2\sigma_s^2$ and $std[U] = 2\sigma_s^2/\sqrt{NL}$. Note that the shape-rate parametrization is used here. To validate the theoretical distribution of U in (19), 360 mechanical stirrer positions (as N) and 401 frequency points between 3.475 GHz and 3.525 GHz (as L) are collected. Note that different antenna positions, orientations, polarizations, *etc.* can also be used. Here, an indirect approach is adopted by separately verifying $\langle P_s(l) \rangle_N \sim Gamma\left(N, N/2\sigma_s^2\right)$ and $\langle P_s(l) \rangle_L \sim Gamma\left(L, L/2\sigma_s^2\right)$. Subsequently, (19) can be proved by the summation and scaling properties of gamma distribution. The benefit of doing this is that while examining one stirring technique, the other can be used for generating samples without using a third stirring technique. The relevant CDF plots are shown in Fig. 3. One thing should be mentioned is that the shape parameter controls the overall shape of a gamma distribution. Hence, the theoretical CDF only fit well with the measured CDF with proper shape parameter value (360 for Fig. 3 (a) and 155 for Fig. 3 (b)). This also implies an effective alternative method for estimating the number of independent samples in addition to the widely-used autocorrelation/autocovariance function method, as will be compared and discussed later.
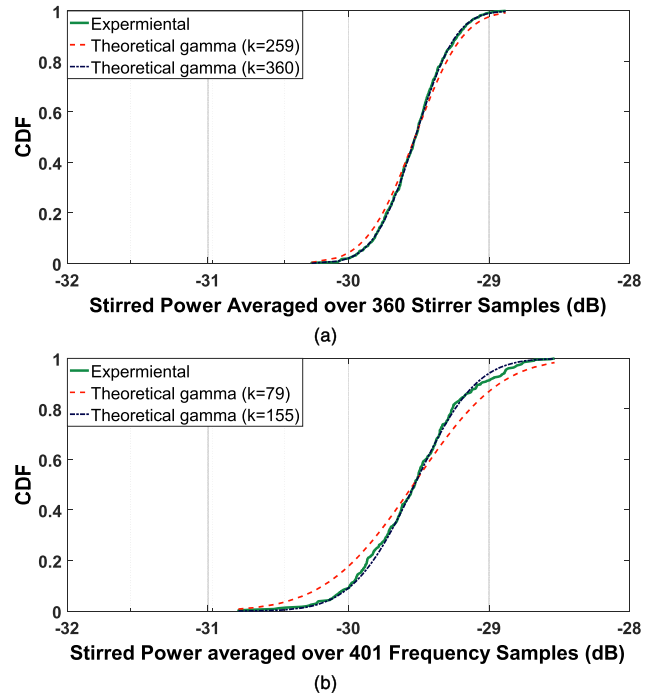
Similarly, following (14), we have

$$V \sim Gamma\left(L, L/2\sigma_{us}^2\right) \quad (20)$$

with $E[V] = 2\sigma_{us}^2$ and $std[V] = 2\sigma_{us}^2/\sqrt{L}$.

Therefore, regarding [34], $\hat{K}_{avg}$ follows a generalized beta prime distribution with three shape parameters L, NL, and 1, and one scale parameter NK_{avg}:

$$\hat{K}_{avg} \sim \beta'\left(L, NL, 1, NK_{avg}\right) \quad (21)$$

Specifically,

$$E\left[\hat{K}_{avg}\right] = \frac{NL}{NL-1} \cdot K_{avg}$$

$$std\left[\hat{K}_{avg}\right] = \frac{NL}{NL-1}\sqrt{\frac{L+NL-1}{L(NL-2)}} \cdot K_{avg} \quad (22)$$

Actually, $\hat{K}_{avg}$ is an asymptotically unbiased estimator of K_{avg}, and its relative uncertainty (also known as the coefficient of variation) is defined as:

$$\tilde{u}\left[\hat{K}_{avg}\right] = \frac{std\left[\hat{K}_{avg}\right]}{E\left[\hat{K}_{avg}\right]} = \sqrt{\frac{L+NL-1}{L(NL-2)}} \quad (23)$$

Nevertheless, it is quite unlikely in practice that samples of $S_{21,us}$ can be directly acquired, and (23) does not reflect the uncertainty introduced by estimating $S_{21,us}$, either. Still,

the formulation of (18) can offer insight into the distribution characteristics of each component.

C. ESTIMATOR OF K_{avg} BASED ON THE MLE METHOD

Now we consider a more practical implementation in which MLEs (4), (5), (10) and (11) are used for inferring the relevant quantities. Then the estimator of K_{avg} can be formulated as

$$\hat{K}'_{avg} = \frac{V'}{U'} = \frac{\left\langle \hat{P}_{us}(l) \right\rangle_L}{\left\langle \hat{P}_{s,avg}(l) \right\rangle_L} \qquad (24)$$

Based on (4) and (10), we have

$$\hat{\mu}_*(l) \sim \mathcal{N}\left(\mu_*(l), \sigma_s^2/N\right) \qquad (25)$$

a gaussian distribution with mean $\mu_*(l)$ and variance σ_s^2/N, and

$$\frac{N}{\sigma_s^2}\hat{\mu}_*^2(l) \sim \chi_1^2\left(N\mu_*^2(l)/\sigma_s^2\right) \qquad (26)$$

a noncentral chi-square distribution with 1 degree of freedom (DoF) and the noncentrality parameter $N\mu_*^2(l)/\sigma_s^2$. Thus, according to the additivity property of chi-square distribution, it is easy to derive that

$$\frac{NL}{\sigma_s^2}V' \sim \chi_{2L}^2\left(2NLK_{avg}\right) \qquad (27)$$

Following (5) and (11), we can get

$$\frac{1}{\sigma_s^2}\sum_{n=1}^N \left|S_{21}^*(l) - \hat{\mu}_*(l)\right|^2 \sim \chi_{N-1}^2(0) \qquad (28)$$

a central chi-square distribution with $N-1$ DoF. Therefore,

$$\frac{L(N-1)}{\sigma_s^2}U' \sim \chi_{2L(N-1)}^2(0) \qquad (29)$$

Combining (24), (27) and (29), one can conclude that

$$N\hat{K}'_{avg} = \frac{\frac{NV'}{2\sigma_s^2}}{\frac{U'}{2\sigma_s^2}} \sim F'_{2L,2L(N-1)}\left(2NLK_{avg}\right) \qquad (30)$$

a noncentral F distribution with $2L$ and $2L(N-1)$ DoFs, and noncentrality parameter $2NLK_{avg}$ [34]. The mean and standard deviation of $\hat{K}'_{avg}$ can be obtained accordingly as:

$$E\left[\hat{K}'_{avg}\right] = \frac{L(N-1)}{NL-L-1}\left(\frac{1}{N} + K_{avg}\right) \qquad (31)$$

$$std\left[\hat{K}'_{avg}\right] = \sqrt{\frac{L^2(N-1)^2(1+NK_{avg})^2}{N^2(NL-L-1)^2(NL-L-2)} + \frac{L(N-1)^2(1+2NK_{avg})}{N^2(NL-L-1)(NL-L-2)}} \qquad (32)$$

Unsurprisingly, when $L = 1$, (31) and (32) degenerate to (5) and (6) in [30].

In order to further investigate the statistical properties of $\hat{K}'_{avg}$, three 10000-sample Monte Carlo simulations with different value combinations of N and L are performed, with parameter settings $P_{s,avg} = -20$ dB and $P_{us,avg} = -40$ dB
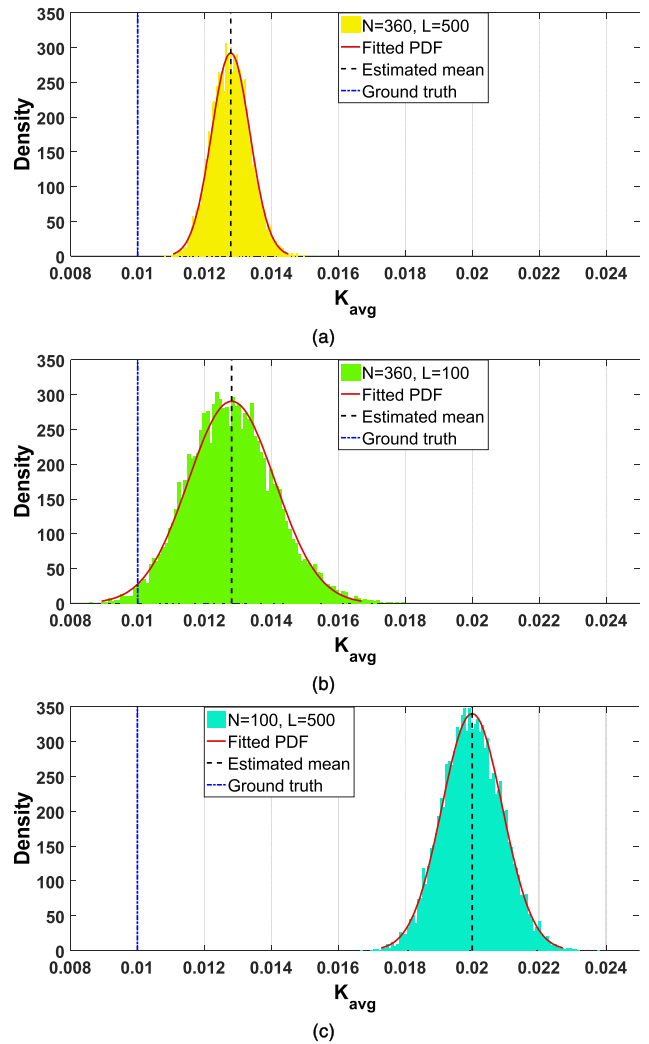

FIGURE 4. Monte Carlo simulation results of sample distributions of the MLE estimator $\hat{K}'_{avg}$ with different *N* and *L* combinations (a) *N* = 360, *L* = 500. (b) *N* = 360, *L* = 100. (c) *N* = 100, *L* = 500. In each subplot, the black dashed line indicates the estimated mean, while the blue dash-dot line indicates the ground truth.

($K_{avg} = -20$ dB). The resulting histograms and fitted PDFs are shown in Fig. 4. In all three scenarios, the clear discrepancies between the estimated means and the ground truth value indicate that $\hat{K}'_{avg}$ is biased, tending to give overestimated results. While N dominates the bias of mean (0.0028 for (a) and (b), and 0.0100 for (c)), both N and L affect the dispersion of samples. Smaller N and L lead to larger variance. It is also interesting to note that the fitted distributions tend to be of symmetrical bell shape, since the DoFs in (30) are large in all three cases.

Next, we construct the unbiased estimator $\hat{K}''_{avg}$ as follows

$$\hat{K}''_{avg} = \frac{NL-L-1}{L(N-1)}\hat{K}'_{avg} - \frac{1}{N} \qquad (33)$$
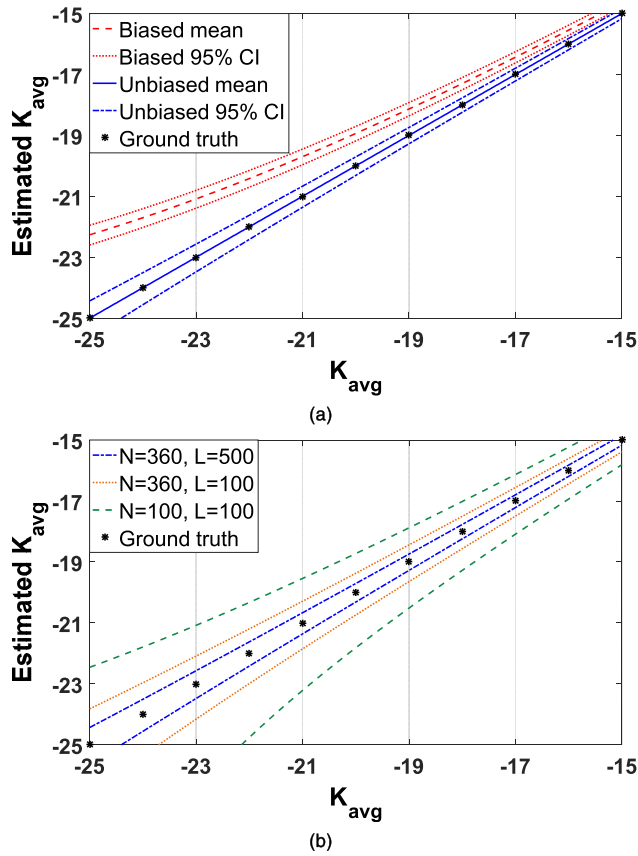
FIGURE 5. (a) Comparison of simulated results of estimators $\hat{K}'_{avg}$ and $\hat{K}''_{avg}$ in the region $K_{avg} \epsilon [-25, -15]$ dB with $N = 360$ and $L = 500$. (b) Comparison of expanded uncertainty intervals (95% CI) of $\hat{K}''_{avg}$ with different N and L combinations in the region $K_{avg} \epsilon [-25, -15]$ dB.

so that $E[\hat{K}''_{avg}] = K_{avg}$, and its standard deviation can be derived as

$$
std \left[\hat{K}''_{avg} \right]
= \sqrt{ \frac{L \left(1 + NK_{avg}\right)^2 + (NL - L - 1)\left(1 + 2NK_{avg}\right)}{LN^2 \left(NL - L - 2\right)} }
\tag{34}
$$

Simulated estimation results of $\hat{K}'_{avg}$ and $\hat{K}''_{avg}$, and their corresponding expanded uncertainty regions (95% confidence interval (CI)) [35] with $N = 360$ and $L = 500$ as a function of the ground truth value from -25 dB to -15 dB are illustrated in Fig. 5 (a). As already pointed out in Fig. 4, $\hat{K}'_{avg}$ results in overestimation. Moreover, this bias becomes more significant as K_{avg} decreases. For example, at -19 dB the discrepancy is less than 1 dB, while at -23 dB it increases to around 2 dB. $\hat{K}''_{avg}$, on the other hand, always makes the correct estimation, but at the expense of slightly increased uncertainty. Fig. 5 (b) demonstrates how N and L affect the performance of $\hat{K}''_{avg}$. As expected, increasing the number of independent stirrer samples and number of independent realizations can effectively reduce the estimation uncertainty. Another thing worth noting is that for fixed N and L values, the estimation uncertainty of $\hat{K}''_{avg}$ tends to become worse with

declining K_{avg}, which implies that more efforts need to be made in order to accurately estimate lower K_{avg} value.

It should be stressed that in [29]–[31] the main focus is the single-case Rician *K*-factor whose definition is given in (6). At adjacent uncorrelated frequency points, the *K*-factor can be treated as i.i.d. Therefore, when averaged, the new estimator (which is essentially the sample mean) has the exact same mean but the standard uncertainty is reduced to $1/\sqrt{F}$ of the original value (as shown in (14) and (15) in [30]). By contrast, this work is about the average Rician *K*-factor defined in (13). The number of frequencies as well as the number of antenna positions, orientations, and polarizations are regarded as realizations that can provide randomness to the unstirred part (see (12) and (14)), and their effect on the mean and standard deviation of $\hat{K}''_{avg}$ can be precisely and exactly reflected in (33) and (34).

III. PROCEDURES OF TRP MEASUREMENT AND ANALYTICAL UNCERTAINTY EXPRESSION USING K_{avg}

A. CALIBRATION STAGE

Typical RC-based TRP measurement generally comprises two stages [15], [27], [36], namely 1) the calibration stage and 2) the measurement stage. In the calibration stage, the chamber transfer function (G_{Cal}, also known as the chamber insertion loss) at the frequency band of interest is estimated between the reference antenna and the measurement antenna. The two antennas are connected to Port 1 and Port 2 of the VNA through cables. If the standard 2-Port calibration is performed, the reference planes are shifted to the inputs of the two antennas (illustrated by the red dashed lines in Fig. 1). Thus, the corrected chamber transfer function can be estimated by

$$
\hat{G}_{Cal} = \frac{\left\langle |S_{21}|^2 \right\rangle_{N_1, L_1}}{\eta_{t, Ref} \, \eta_{t, Meas}}
\tag{35}
$$

where $\eta_{t, Ref}$ and $\eta_{t, Meas}$ are the total efficiencies of the reference antenna and the measurement antenna, respectively. We follow the convention in Section II to use $L_1 = F_1 \cdot M_1$ for notational convenience, where F_1 and M_1 denote the numbers of independent frequency points and independent source locations used in the calibration stage. In addition, N_1 is the number of independent stirrer samples adopted in this stage.

B. MEASUREMENT STAGE

As for the measurement stage, the reference planes are indicated by the green dashed lines in Fig. 1. The DUT is radiating at its maximum power, and the measurement antenna is connected to the SA through the measurement cable. Then the averaged receiving power read from the SA can be expressed as

$$
\left\langle P_{SA} \right\rangle_{N_2} = P_{DUT} \hat{G}_{Meas} \eta_{t, Meas} L_{Meas}
\tag{36}
$$

where P_{DUT} is the unknown TRP of the DUT to be inferred, $\hat{G}_{Meas}$ is the equivalent estimated chamber transfer function

in the measurement stage (which cannot be directly obtained), L_{Meas} is the loss of the measurement cable, and N_2 is the number of independent stirrer samples used in this stage. Note that frequency stirring is not applicable in the measurement stage ($F_2 = 1$) since the radiating property of the wireless device might be quite different at different frequencies (depending upon the specific protocol) [37]. Based on (35), (36), and the assumption that $\hat{G}_{Cal} = \hat{G}_{Meas}$, the TRP estimator of the DUT can be formulated as

$$\hat{P}_{DUT} = \frac{\eta_{t,Ref}}{L_{Meas}} \cdot \frac{\langle P_{SA} \rangle_{N_2}}{\langle |S_{21}|^2 \rangle_{N_1,L_1}} = \alpha \cdot \frac{Y}{X} \tag{37}$$

α can be treated as a constant if datasheets of the corresponding quantities are available. In contrast, X and Y are two independent random variables, and individual relative uncertainties should be combined in quadrature and propagated to $\hat{P}_{DUT}$ [38] as

$$\tilde{u}\left[\hat{P}_{DUT}\right] = \sqrt{\tilde{u}^2\left[X\right] + \tilde{u}^2\left[Y\right]} \tag{38}$$

C. ANALYTICAL UNCERTAINTY EXPRESSION BASED ON K_{avg}

As already indicated in (37), when measuring the TRP of a wireless device, only scalar information (the receiving power measured by the SA, or equivalently $|S_{21}|^2$) is obtainable. As a result, the uniformity issue cannot be directly compensated [24]. To overcome this problem, various uncertainty models adopt the explicit representation of the Rician K-factor so as to quantify the effect of the lacking of spatial uniformity [11], [20]–[22]. Based on (17) in [20] which utilizes a components-of-variance model and by doing the following: 1) extend the model from K to K_{avg}; 2) neglect the effect of measurement perturbation (*e.g.*, noise, imperfection of calibration, and cable movement); 3) correct sample correlations by estimating the independent sample number for each stirring technique utilized; and 4) combine uncertainties in both the calibration stage and the measurement stage using (38), we can derive the overall analytical uncertainty model for TRP measurement in an RC as:

$$\tilde{u}_{ana}\left[\hat{P}_{DUT}\right] = \sqrt{\begin{array}{c} \frac{\frac{1}{N_1 L_1} + \frac{2}{N_1 L_1} K_{avg} + \frac{1}{M_1} K_{avg}^2}{(1 + K_{avg})^2} \\ + \frac{\frac{1}{N_2} + \frac{2}{N_2} K_{avg} + K_{avg}^2}{(1 + K_{avg})^2} \end{array}} \tag{39}$$

In reality, K_{avg} should be replaced by the corrected MLE estimator $\hat{K}_{avg}''$. Regarding (39) it is clear that, with the intention of achieving low measurement uncertainty, the number of independent samples used in each stage should be large, and K_{avg} should be kept small. Specifically, when K_{avg} is so small that it is negligible, (39) reduces to a baseline model:

$$\tilde{u}_{BL} = \sqrt{\frac{1}{N_1 L_1} + \frac{1}{N_2}} \tag{40}$$

Fig. 6 illustrates the comparison result of the proposed analytical model (39) and the baseline model (40) with $N_1 =$
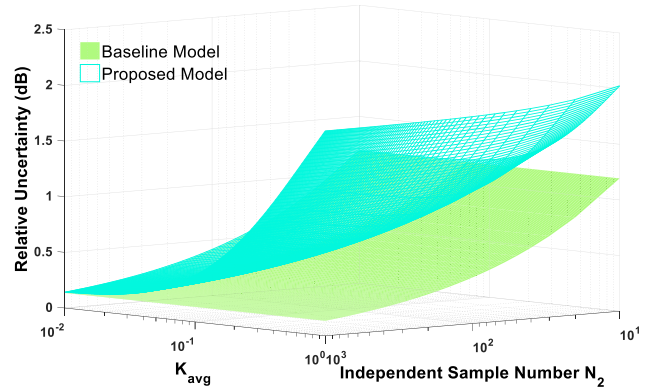

FIGURE 6. Comparison of analytical models (39) and (40) as a function of $K_{avg} \epsilon [-20, 0]$ dB and $N_2 \epsilon [10, 1000]$ with $N_1 = 360$, $F_1 = 158$ and $M_1 = 9$.

360 and $L_1 = 1422$ ($F_1 = 158$ and $M_1 = 9$) as a function of the K_{avg} (-20 dB – 0 dB) and N_2 (10 – 1000). As K_{avg} increases, its adverse effect on the measurement uncertainty becomes more prominent. Consequently, the baseline model (40) tends to significantly underestimate the uncertainty and renders overly optimistic predictions. In addition, using larger N_2 value during the measurement stage seems to magnify this impact.

IV. MEASUREMENTS

In this section, the TRP of the DUT is measured following the procedures described in Section III. The relative measurement uncertainty is then empirically estimated using the 9-Point approach [15], [21], [23], and the results are compared to that directly predicted by the analytical uncertainty model (39) for assessment. Methods for derivation of relevant parameters present in (39) are also explained.

A. EXPERIMENTAL SETUP AND PREPARATIONS

Measurements are conducted using the RC at the University of Liverpool, which has a size of 3.60 m (*w*)× 5.80 m (*l*)× 4.00 m (*h*). Fig. 7 (a) shows the interior of the RC and the typical measurement setup. One horizontal stirrer (with rotating radius 0.50 m) and one vertical stirrer (with rotating radius 0.70 m) with asymmetrical paddles are installed at the opposite corners inside the RC. During the mechanical stirring process, the two stirrers are synchronized by the motor controller so that they rotate simultaneously in mode-tuning mode. A rotating platform (1.52 m high) is used for mounting the reference antenna/DUT, and a tripod with 1.40 m in height is utilized for supporting the measurement antenna. In order to minimize the LOS and the unstirred NLOS components, the reference antenna/DUT and the measurement antenna should be directed away from each other and towards different stirrers. As depicted in Fig. 7 (b), T1 through T9 represent the 9 locations of the reference antenna/DUT for applying source stirring or 9-Point uncertainty estimation. The measurement antenna, by contrast, is fixed at the point labelled "Meas.". Useful distance information is also available in

TABLE 1. Configuration information and parameter specification for TRP measurement and estimation of the relative uncertainty.

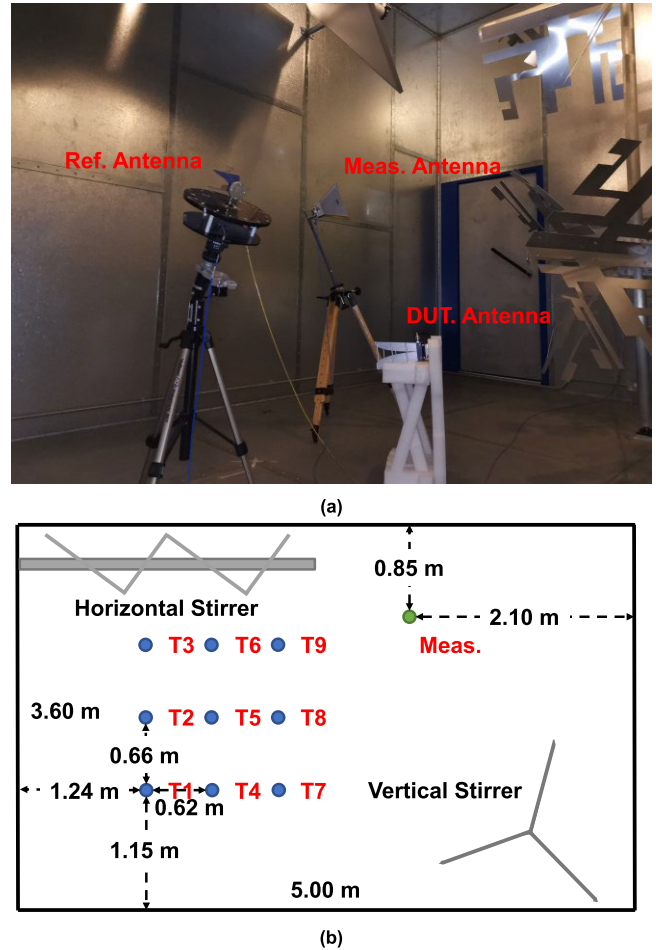| Stage	Quality	Value
Calibration	Frequency range	3.475 GHz – 3.525 GHz
	Number of frequency points	401
	Frequency domain resolution	125 kHz
	Number of stirrer positions	360
	Stirrer step size	1°
	Number of source locations	9
	Equipment	VNA
	Ref. antenna bandwidth	2 GHz – 32 GHz
	Ref. antenna efficiency	-0.46 dB (89.95%)
Measurement	Carrier frequency	3.5 GHz
	Number of stirrer positions	10, 20, 30, 60, 90, 120, 180, 360
	Stirrer step size	36°, 18°, 12°, 6°, 4°, 3°, 2°, 1°
	Equipment	SG & SA
	DUT antenna bandwidth	1 GHz – 18 GHz
	DUT antenna efficiency	-0.44 dB (90.36%)
	Output power of the SG	3 dBm
	Ref. cable loss at 3.5 GHz	-6.71 dB
	Nominal TRP of the DUT	-4.15 dBm
Common settings	IF bandwidth	10 kHz
	Meas. antenna bandwidth	1 GHz – 18 GHz
	Meas. cable loss at 3.5 GHz	-6.29 dB
	Idle mode termination	50 Ω

(a)

(b)

FIGURE 7. Experimental setup for TRP measurement and uncertainty assessment procedures: (a) Measurement scenario inside the RC at the University of Liverpool. (b) Schematic diagram of the top view showing the 9 locations for the reference antenna/DUT and the fixed position for the measurement antenna.

Fig. 7 (b). Throughout the whole measurement process, the reference antenna, the DUT, and the measurement antenna should all be placed inside the RC so that the loading condition of the RC (and thus the composite quality factor) remains unchanged. The reference antenna or the DUT which is in idle mode should be terminated with a 50 Ω load.

Detailed configuration information and parameter specification for the calibration stage and the measurement stage is summarized in Table 1. The n78 band which belongs to the 5G frequency range 1 (FR1) [39] with 3.5 GHz carrier frequency is selected for the experiment. In the calibration stage a 50 MHz frequency sweeping (3.475 GHz – 3.525 GHz with 125 kHz frequency resolution) is performed using an Agilent N9917A FieldFox VNA, while in the measurement stage only the single carrier point is measured by a Keithley 2820 SA. A Rohde & Schwarz HF 906 antenna is used as the reference antenna, and the measurement antenna is of type SATIMO SH 2000. An SG (Keithley 2920, used as the power source), an MVG SH1000 dual-ridge horn antenna (used as the radiator), and the cable (the Ref. cable as sketched in Fig. 1) connecting them together is considered as an "combined" DUT. The output power of the SG is set to 3 dBm (3.5 GHz single tone), and the total efficiency of the radiating antenna and the insertion loss of the Ref. cable are -0.44 dB and -6.71 dB respectively at 3.5 GHz. Therefore, the nominal TRP of this DUT is -4.15 dBm (this also ensures the consistency of the reference plane "Meas. RP1" as shown in Fig. 1). Multiple configurations of stirrer positions and step angles are used to repeat the measurement stage so that the

relative uncertainty as a function of N_2 can be illustrated and examined.

B. CALIBRATION STAGE

1) ESTIMATION OF THE NUMBER OF INDEPENDENT STIRRER POSITION, FREQUENCY, AND SOURCE LOCATION SAMPLES

The autocovariance of the transmission coefficient S_{21} as a function of the offset angle $\partial\theta$ of the stirrer positions is defined as:

$$C\left(\partial\theta, f\right) = \int_{-\Theta}^{+\Theta} \left(S_{21}(\theta, f) - \langle S_{21}(\theta, f)\rangle_{\Theta}\right) \\ \left(S_{21}^{*}(\theta + \partial\theta, f) - \langle S_{21}^{*}(\theta, f)\rangle_{\Theta}\right) d\theta \quad (41)$$

where the superscript $*$ is the complex conjugate notation, and f denotes frequency (3.5 GHz in this case). A whole stirrer revolution ($\Theta = 360°$) is considered with 1° step size, and $\theta + \partial\theta$ is processed by the modulo 360 operation. Then (41) is normalized by its maximum value and averaged over the
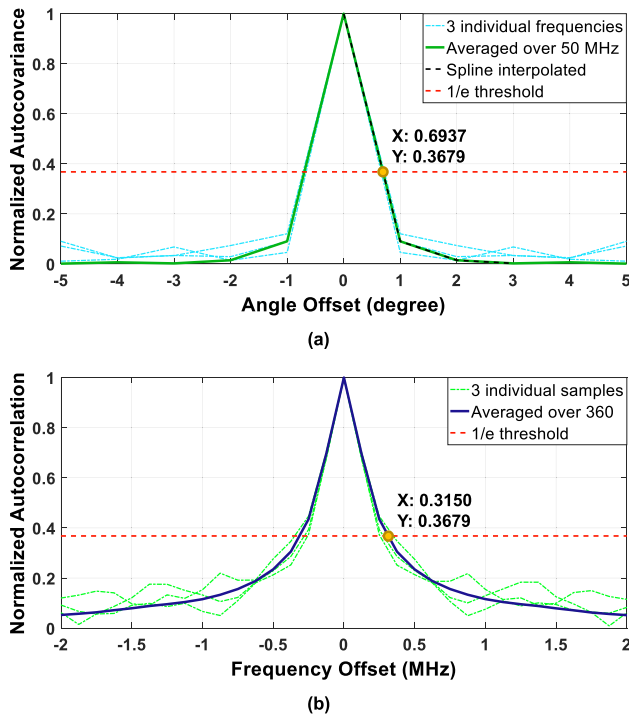
FIGURE 8. (a) Estimation of the number of independent stirrer samples using the normalized autocovariance function averaged over 50 MHz bandwidth. (b) Estimation of the number of independent frequency points using the normalized autocorrelation function averaged over 360 stirrer positions. In both figures, arbitrarily picked individual samples as well as the averaged result are plotted for comparison.

frequency region 3.475 GHz – 3.525 GHz. The result is illustrated in Fig. 8 (a). Note that the cubic spline interpolation is applied around the region of interest to increase the density of points (the black dashed curve). Following the IEC standard [15] with a $1/e$ threshold, the coherence angle is approximately 0.69°, less than the step size between adjacent stirrer positions, which means that all the 360 samples provided by mechanical stirring can be considered as uncorrelated (and equivalently, independent). Therefore, we have $N_1 = 360$.

Similarly, the autocorrelation function in terms of the frequency offset ∂f at a certain stirrer position n is given as:

$$R(\partial f, n) = \int_{f_{start}}^{f_{end}} S_{21}(f, n)S_{21}^*(f + \partial f, n)\, df \quad (42)$$

where $f_{start} = 3.475$ GHz, and $f_{start} = 3.525$ GHz. Fig. 8 (b) plots 3 individual stirrer positions as well as the averaged result over 360 stirrer positions. For the $1/e$ threshold, the coherence bandwidth is 315 kHz, which corresponds to $F_1 = 158$ independent frequency points across a 50 MHz band.

It should be pointed out that Fig. 8 is obtained with the Ref. antenna placed at T1. The same process is also repeated for the other eight locations, and highly close results can be obtained.

Recall Fig. 3, as aforementioned, the task of independent sample number estimation can be converted into a parameter optimization problem aiming at finding the optimum
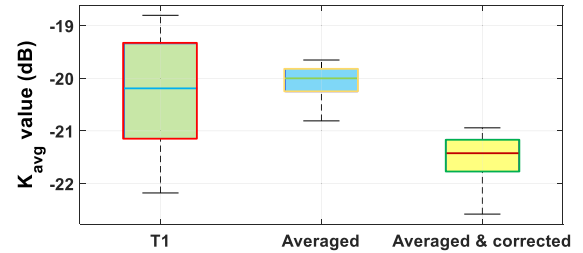

FIGURE 9. Derivation of K_{avg} with $N_1 = 360$, $F_1 = 158$ and $M_1 = 9$ using the MLE estimator (24) and then the result is corrected by (33). Adjacent frequency points are treated as samples for the boxplot. The K-factor estimated at a single source position T1 is also shown for comparison.

shape factor k that minimizes the sum-of-square error (SSE) between the relevant theoretical CDF of the gamma distribution and the measured CDF (we name it the CDF fitting method):

$$\arg\min_k SSE(k) = \arg\min_k [CDF_{meas} - CDF_{theo}(k)]^2 \quad (43)$$

where the subscript *meas* means "measured", and *theo* means "theoretical". Due to its physical meaning, k should be a positive integer. The numbers of independent stirrer positions and frequency points derived by the CDF fitting method are $N_1 = 360$ and $F_1 = 155$ (as shown in Fig. 3). It can be seen that the two methods give similar results, so they can be used for cross validation for improved estimation accuracy. For consistency's sake, in the following calculations we still adopt the results derived by the autocovariance/autocorrelation method.

As demonstrated in Fig. 7 (b), the minimum separation distance between two adjacent source locations is 0.62 m, which corresponds to approximately 7.23 λ at 3.5 GHz. Therefore, it is reasonable to assume that all the 9 source positions are spatially uncorrelated, *i.e.*, $M_1 = 9$.

2) DERIVATION OF K_{avg} VALUE
As explained in Section II-C, K_{avg} is estimated using the MLE estimator (24) and then corrected by the unbiasing operation (33). With the aim of showing the dispersion of measurement, K_{avg} at adjacent frequency points are used as i.i.d samples. The resultant boxplots are shown in Fig. 9. It can be found that by utilizing source stirring (so that the unstirred part is considered as random), the uncertainty can be further improved compared with the individual source position case (T1). After the unbiasing operation, the median value of K_{avg} is decreased (also the mean value), but a slight increase in terms of the uncertainty is observed, which is consistent with the simulated results shown in Fig. 5 (a). It can be derived that $\hat{K}_{avg}'' = -21.49$ dB at 3.5 GHz, and this value will be used in subsequent calculations.

3) UNCERTAINTY COMPARISON
In the calibration stage, the transfer function $\hat{G}_{Cal}$ (or equivalently X) is calculated using 360 stirrer positions ($N_1 = 360$), 50 MHz band with frequency step of 125 kHz ($F_1 = 158$)

TABLE 2. ANOVA table.

Source	Sum of Squares	DoF	Mean Square	F-value	P-value
Between	3.96×10^{-7}	8	4.95×10^{-8}		
Within	2.90×10^{-5}	3231	8.98×10^{-9}	5.51	6.06×10^{-7}
Total	2.94×10^{-5}	3239	—		

and 9 reference antenna locations ($M_1 = 9$). The uncertainty is first directly estimated by the 9-Point method, and then analytically calculated using the proposed model (39) and the bassline model (40) for comparison. Note that up to now we only consider about the calibration stage, so only the first term of (39) and (40) in the square root is used.

In order to select the appropriate equation for the 9-Point uncertainty estimation procedure, the one-way analysis of variance (ANOVA) test, which examines whether the means of multiple sample groups are equal or not by comparing the between and within variances [21], [38], is performed. Details of how to form the sum of squares between (SSB), the sum of squares within (SSW), and the relevant F statistic are omitted here. The test result is listed in Table 2. Since the P-value (6.06×10^{-7}) is much smaller than the 0.05 significance level, the impact of lacking of spatial uniformity dominates the uncertainty, and the null hypothesis that "all sample groups (transfer functions calculated at each of the nine locations T1–T9) have identical mean value" should be rejected. Consequently, (44) should be used for assessing the relative uncertainty [21].

$$\tilde{u}_{est}[X] = \frac{\sqrt{\sum_{m=1}^{M_1} \left(\langle |S_{21}(m)|^2 \rangle_{N_1, F_1} - X \right)^2}}{\sqrt{M_1(M_1 - 1)} X} \quad (44)$$

It should be stressed that the 9 source positions are also used as source stirring samples for calculating X. That is why there is a $\sqrt{M_1}$ term in the denominator of (44).

Comparison between the estimated and analytical models is shown in Table 3. Since a very large set of independent samples is utilized (511920 as derived in Section IV-B-1)), all the three methods give low relative uncertainty values. The baseline model (40) leads to underestimated result, while the proposed model (39) can make effective improvement even in an environment with extremely low K_{avg} value (-21.49 dB). Apart from finite number of independent samples and limited spatial uniformity, there might be other sources of uncertainty such as imperfect 2-Port calibration, cable movement, VNA stability, etc. This partially explains the discrepancy between the estimated result (0.37%) and the proposed analytical result (0.27%).

The resultant transfer function is $X = -29.53$ dB, which will be used in the measurement stage.

C. MEASUREMENT STAGE
In this stage, the TRP of the DUT is measured, and the overall relative uncertainty considering both stages is estimated and

TABLE 3. Table of comparison between estimated and analytical relative uncertainties in the calibration stage.

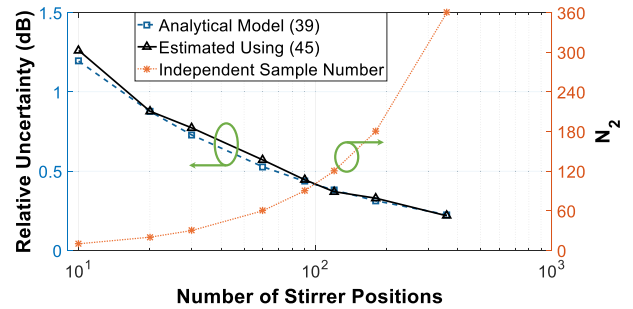| N_1=360, F_1=158, and M_1=9	Relative Uncertainty
9-Point estimation	0.37%
Proposed model (39) (calibration stage only)	0.27%
Baseline model (40) (calibration stage only)	0.14%

FIGURE 10. Comparison of the overall estimated and proposed analytical relative uncertainties as a function of N_2 at 3.5 GHz.

compared with that theoretically calculated using the proposed model (39). After N_2 samples of P_{SA} are collected by the SA, its sample mean Y can be derived, and (37) is utilized to calculate $\hat{P}_{DUT}$. This procedure is performed nine times with the DUT placed at T1–T9. At each source location, the orientation of the DUT is intentionally configured to be different from that of the reference antenna during the calibration stage. The empirical relative uncertainty is calculated according to the following equation:

$$\tilde{u}_{est}\left[\hat{P}_{DUT}\right] = \frac{\sqrt{\sum_{m=1}^{M_1} \left(\hat{P}_{DUT}(m) - \langle \hat{P}_{DUT} \rangle_{M_1} \right)^2}}{\sqrt{(M_1 - 1)} \langle \hat{P}_{DUT} \rangle_{M_1}} \quad (45)$$

Then the measurement stage is repeated with various N_2 values (as specified in Table 1). The comparison result as a function of N_2 is demonstrated in Fig. 10. The linear to decibel transformation defined in [15]

$$\tilde{u}_{dB} = 10 \log_{10}(1 + \tilde{u}) \quad (46)$$

is adopted for illustration purpose. It can be found that both $\tilde{u}_{est}\left[\hat{P}_{DUT}\right]$ and $\tilde{u}_{ana}\left[\hat{P}_{DUT}\right]$ monotonically decrease with increasing N_2. Generally speaking, the two uncertainty curves are in good agreement with each other, although the estimated one is slightly higher. The reason is similar to that in the calibration stage. The measurement process is also repeated with the DUT located at nine positions different from T1–T9 (but still within the working volume), and the result is comparable with that shown in Fig. 10.

Next, the whole process is redone at two additional carrier frequencies (3.45 GHz and 3.55 GHz) within the n78 band. The 50 MHz offset from the original 3.5 GHz carrier frequency guarantees that it is large enough to be considered as independent, but small enough to assume that the values
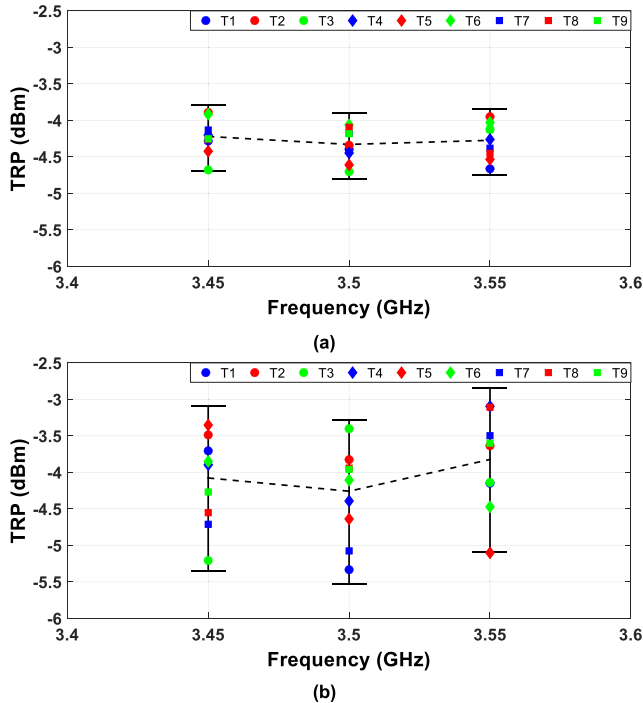
FIGURE 11. Individual $\hat{P}_{DUT}$ measurements at nine source locations T1–T9 at three different carrier frequencies (3.45 GHz, 3.5 GHz, and 3.55 GHz) with corresponding expanded relative uncertainties (95% CI) calculated using the proposed analytical model (39): (a) $N_2 = 360$. (b) $N_2 = 60$.

of $\eta_{t,Ref}$, L_{Meas}, and L_{Ref} are similar. Typical variations of individual $\hat{P}_{DUT}$ measurements at the three frequencies are shown in Fig. 11 with two measurement stage configurations: $N_2 = 360$ and $N_2 = 60$. The expanded relative uncertainty regions that derived analytically using (39) with a scaling factor of 1.96 are also plotted (centered at the corresponding sample means). By comparing the two subplots, it is easy to see that the larger the value of N_2, the smaller the measurement dispersion, and the smaller the fluctuation of the sample means. However, if more independent samples are used, the measurement time will be longer. That is to say, there is a clear trade-off between measurement accuracy and measurement efficiency. Another thing worth mentioning is that the 95% CIs calculated using (39) fit individual measurements quite well, which verifies that the proposed analytical model is reasonably accurate.

V. CONCLUSION

An improved analytical uncertainty model for OTA TRP measurement in an RC that considered both the sample correlation and the spatial uniformity issues was proposed in this work. The necessity and benefit of using K_{avg} instead of single-case K was elaborated. A thorough statistical analysis for K_{avg} including the formulation of the MLE estimator and its unbiasing correction was conducted, and Monte Carlo simulations were performed for verification of the derived statistics. Good agreement between the proposed analytical model and the estimation through the 9-Point approach demonstrated that the proposed model is reasonably accurate.

The proposed model not only greatly simplifies the work needed for characterizing the measurement dispersion, but also guides the best practice for TRP measurement. It aims at providing satisfactory measurement accuracy while maintaining fast measurement speed. Since the calibration stage is conducted "offline", it is recommended that a large number of independent samples is used with multiple stirring techniques. By contrast, for the measurement stage which is performed "online", there is a trade of between the number of independent samples provided and the measurement efficiency. Therefore, the value of N_2 should be carefully set on demand. In all cases, K_{avg} should be kept small so that good spatial uniformity can be achieved.

Another thing needs to be stressed is that during the experiment, the reference antenna and DUT are both directional and have similar radiation patterns at the frequency band of interest. In practice, for a DUT whose radiation property could be quite different from the reference antenna used in the calibration stage, a slightly higher uncertainty might be observed. How to effectively solve this problem might be a future research direction.

REFERENCES

[1] T. S. Rappaport, S. Sun, R. Mayzus, H. Zhao, Y. Azar, K. Wang, G. N. Wong, J. K. Schulz, M. Samimi, and F. Gutierrez, "Millimeter wave mobile communications for 5G cellular: It will work!" *IEEE Access*, vol. 1, pp. 335–349, 2013.

[2] F. Boccardi, R. W. Heath, Jr., A. Lozano, T. L. Marzetta, and P. Popovski, "Five disruptive technology directions for 5G," *IEEE Commun. Mag.*, vol. 52, no. 2, pp. 74–80, Feb. 2014.

[3] W. Fan, I. Carton, P. Kyosti, A. Karstensen, T. Jamsa, M. Gustafsson, and G. F. Pedersen, "A step toward 5G in 2020: Low-cost OTA performance evaluation of massive MIMO base stations," *IEEE Antennas Propag. Mag.*, vol. 59, no. 1, pp. 38–47, Feb. 2017.

[4] Y. Qi, G. Yang, L. Liu, J. Fan, A. Orlandi, H. Kong, W. Yu, and Z. Yang, "5G over-the-air measurement challenges: Overview," *IEEE Trans. Electromagn. Compat.*, vol. 59, no. 6, pp. 1661–1670, Dec. 2017.

[5] K. A. Remley, J. A. Gordon, D. Novotny, A. E. Curtin, C. L. Holloway, M. T. Simons, R. D. Horansky, M. S. Allman, D. Senic, M. Becker, and J. A. Jargon, "Measurement challenges for 5G and beyond: An update from the national Institute of standards and technology," *IEEE Microw. Mag.*, vol. 18, no. 5, pp. 41–56, Jul./Aug. 2017.

[6] D. A. Hill, *Electromagnetic Fields in Cavities*. Piscataway, NJ, USA: IEEE Press, 2009.

[7] X. Chen, J. Tang, T. Li, S. Zhu, Y. Ren, Z. Zhang, and A. Zhang, "Reverberation chambers for over-the-air tests: An overview of two decades of research," *IEEE Access*, vol. 6, pp. 49129–49143, 2018.

[8] Q. Xu and Y. Huang, *Anechoic and Reverberation Chambers: Theory, Design and Measurements*. Hoboken, NJ, USA: Wiley, 2019.

[9] L. R. Arnaut, "Measurement uncertainty for reverberation chambers-I. Sample statistics," NPL, London, U.K., NPL Rep. TQ 2, Dec. 2008, pp. 1–136.

[10] Y. Huang and D. J. Edwards, "A novel reverberating chamber: The source-stirred chamber," in *Proc. Int. Conf. Electromagn. Compat.*, Edinburgh, U.K., Sep. 1992, pp. 120–124.

[11] P.-S. Kildal, X. Chen, C. Orlenius, M. Franzen, and C. S. L. Patane, "Characterization of reverberation chambers for OTA measurements of wireless devices: Physical formulations of channel matrix and new uncertainty formula," *IEEE Trans. Antennas Propag.*, vol. 60, no. 8, pp. 3875–3891, Aug. 2012.

[12] D. A. Hill, "Electronic mode stirring for reverberation chambers," *IEEE Trans. Electromagn. Compat.*, vol. 36, no. 4, pp. 294–299, Nov. 1994.

[13] A. Gifuni, L. Bastianelli, F. Moglie, V. M. Primiani, and G. Gradoni, "Base-case model for measurement uncertainty in a reverberation chamber including frequency stirring," *IEEE Trans. Electromagn. Compat.*, vol. 60, no. 6, pp. 1695–1703, Dec. 2018.

[14] A. Gifuni, L. Bastianelli, M. Migliaccio, F. Moglie, V. Mariani Primiani, and G. Gradoni, ''On the estimated measurement uncertainty of the insertion loss in a reverberation chamber including frequency stirring,'' *IEEE Trans. Electromagn. Compat.*, vol. 61, no. 5, pp. 1414–1422, Oct. 2019.

[15] *Electromagnetic Compatibility (EMC)—Part 4-21: Testing and Measurement Techniques—Reverberation Chamber Test Methods*, IEC Standard IEC 61000-4-21, Ed 2.0, 2011.

[16] *User Equipment (UE) / Mobile Station (MS) Over The Air (OTA) Antenna Performance; Conformance Testing*, Standardtd. TS 34.114, Rev. V12.2.0, 3GPP, Sep. 2016.

[17] *Test Plan for Wireless Large-Form-Factor Device Over-the-Air Performance*, CTIA, Washington, DC, USA, ver. 1.2.1, Feb. 2019.

[18] *Radio Frequency (RF) Conformance Testing Background for Radiated Base Station (BS) Requirements*, Standard TR 37.941, Rev. V16.0.1, 3GPP, Jun. 2020.

[19] R. J. Pirkl, K. A. Remley, and C. S. L. Patane, ''Reverberation chamber measurement correlation,'' *IEEE Trans. Electromagn. Compat.*, vol. 54, no. 3, pp. 533–545, Jun. 2012.

[20] K. A. Remley, R. J. Pirkl, H. A. Shah, and C.-M. Wang, ''Uncertainty from choice of mode-stirring technique in reverberation-chamber measurements,'' *IEEE Trans. Electromagn. Compat.*, vol. 55, no. 6, pp. 1022–1030, Dec. 2013.

[21] K. A. Remley, C.-M.-J. Wang, D. F. Williams, J. J. aan den Toorn, and C. L. Holloway, ''A significance test for reverberation-chamber measurement uncertainty in total radiated power of wireless devices,'' *IEEE Trans. Electromagn. Compat.*, vol. 58, no. 1, pp. 207–219, Feb. 2016.

[22] D. Senic, K. A. Remley, C.-M.-J. Wang, D. F. Williams, C. L. Holloway, D. C. Ribeiro, and A. T. Kirk, ''Estimating and reducing uncertainty in reverberation-chamber characterization at millimeter-wave frequencies,'' *IEEE Trans. Antennas Propag.*, vol. 64, no. 7, pp. 3130–3140, Jul. 2016.

[23] K. A. Remley, J. Dortmans, C. Weldon, R. D. Horansky, T. B. Meurs, C.-M. Wang, D. F. Williams, C. L. Holloway, and P. F. Wilson, ''Configuring and verifying reverberation chambers for testing cellular wireless devices,'' *IEEE Trans. Electromagn. Compat.*, vol. 58, no. 3, pp. 661–672, Jun. 2016.

[24] K. A. Remley, R. J. Pirkl, C.-M. Wang, D. Senic, A. C. Homer, M. V. North, M. G. Becker, R. D. Horansky, and C. L. Holloway, ''Estimating and correcting the device-under-test transfer function in loaded reverberation chambers for over-the-air tests,'' *IEEE Trans. Electromagn. Compat.*, vol. 59, no. 6, pp. 1724–1734, Dec. 2017.

[25] M. G. Becker, M. Frey, S. Streett, K. A. Remley, R. D. Horansky, and D. Senic, ''Correlation-based uncertainty in loaded reverberation chambers,'' *IEEE Trans. Antennas Propag.*, vol. 66, no. 10, pp. 5453–5463, Oct. 2018.

[26] X. Chen, ''Measurement uncertainty of RC and its reduction techniques for OTA tests: A review,'' *IET Microw., Antennas Propag.*, vol. 13, no. 15, pp. 2598–2604, Dec. 2019.

[27] W. Xue, F. Li, X. Chen, and T. Svensson, ''Statistical analysis of measurement uncertainty in total radiated power of wireless devices in reverberation chamber,'' *IET Microw., Antennas Propag.*, vol. 14, no. 11, pp. 1241–1245, Sep. 2020.

[28] C. L. Holloway, D. A. Hill, J. M. Ladbury, P. F. Wilson, G. Koepke, and J. Coder, ''On the use of reverberation chambers to simulate a rician radio environment for the testing of wireless devices,'' *IEEE Trans. Antennas Propag.*, vol. 54, no. 11, pp. 3167–3177, Nov. 2006.

[29] C. Lemoine, E. Amador, and P. Besnier, ''On the *K*-factor estimation for Rician channel simulated in reverberation chamber,'' *IEEE Trans. Antennas Propag.*, vol. 59, no. 3, pp. 1003–1012, Mar. 2011.

[30] C. M. J. Wang, K. A. Remley, A. T. Kirk, R. J. Pirkl, C. L. Holloway, D. F. Williams, and P. D. Hale, ''Parameter estimation and uncertainty evaluation in a low rician K-Factor reverberation-chamber environment,'' *IEEE Trans. Electromagn. Compat.*, vol. 56, no. 5, pp. 1002–1012, Oct. 2014.

[31] A. Gifuni and S. Perna, ''K-factor estimate: Statistical behavior of its distribution for large sample sizes,'' *IEEE Trans. Electromagn. Compat.*, vol. 61, no. 6, pp. 1896–1899, Dec. 2019.

[32] X. Chen, P.-S. Kildal, and J. Carlsson, ''Investigation of the distribution of the random LOS component in a reverberation chamber,'' in *Proc. Eur. Conf. Antennas Propag. (EuCAP)*, Gothenburg, Sweden, Apr. 2013, pp. 8–12.

[33] X. Chen, P.-S. Kildal, and S.-H. Lai, ''Estimation of average Rician K-factor and average mode bandwidth in loaded reverberation chamber,'' *IEEE Antennas Wireless Propag. Lett.*, vol. 10, pp. 1437–1440, 2011.

[34] N. L. Johnson and S. Kotz, *Continuous Univariate Distributions*, vol. 2, 2nd ed. New York, NY, USA: Wiley, 1995.

[35] A. Papoulis, *Probability, Random Variables, and Stochastic Processes*. New York, NY, USA: McGraw-Hill, 1965.

[36] Q. Xu, Y. Huang, S. Yuan, L. Xing, and Z. Tian, ''Two alternative methods to measure the radiated emission in a reverberation chamber,'' *Int. J. Antennas Propag.*, vol. 2016, pp. 1–7, Jan. 2016.

[37] J. C. West and C. F. Bunting, ''Effects of frequency stirring on reverberation chamber testing: An analysis as a radiation problem,'' *IEEE Trans. Electromagn. Compat.*, vol. 61, no. 4, pp. 1345–1352, Aug. 2019.

[38] B. N. Taylor and C. E. Kuyatt, ''Guidelines for evaluating and expressing the uncertainty of NIST measurement results,'' NIST, Gaithersburg, MD, USA, Tech. Rep. NIST Tech. 1297, Sep. 1994.

[39] *NR; User Equipment (UE) Radio Transmission and Reception; Part 1: Range 1 Standalone*, Standard TS 38.101-1, Rev. V16.4.0, 3GPP, Jun. 2020.

TIANYUAN JIA received the B.Eng. degree in telecommunications engineering from Xi'an Jiaotong-Liverpool University (XJTLU), Suzhou, China, in 2012, and the M.Sc. degree in communications and signal processing from Imperial College London, London, U.K., in 2013. He is currently pursuing the Ph.D. degree in electrical engineering and electronics with the University of Liverpool, Liverpool, U.K. His current research interests include reverberation chamber measurement techniques, 5G over-the-air testing, propagation channel modeling and emulation, electromagnetic compatibility testing, statistical electromagnetics, and localization techniques.

YI HUANG (Senior Member, IEEE) received the B.Sc. degree in physics from Wuhan University, China, in 1984, the M.Sc. (Eng) in microwave engineering from NRIET, Nanjing, China, in 1987, and the D.Phil. degree in communications from the University of Oxford, U.K., in 1994. He has been conducting research in the areas of wireless communications, applied electromagnetics, radar, and antennas since 1987. His experience includes three years spent with NRIET as a Radar Engineer and various periods with the Universities of Birmingham, Oxford, and Essex, U.K., as a member of the research staff. He worked as a Research Fellow at British Telecom Labs in 1994, and then joined the Department of Electrical Engineering & Electronics, University of Liverpool, U.K., as a faculty in 1995, where he is currently a Full Professor in Wireless Engineering, the Head of the High-Frequency Engineering Group, and the Deputy Head of the Department. He has published over 350 refereed papers in leading international journals and conference proceedings, and authored *Antennas: from Theory to Practice* (John Wiley, 2008) and *Reverberation Chambers: Theory and Applications to EMC and Antenna Measurements* (John Wiley, 2016). He has received many research grants from research councils, government agencies, charity, EU, and industry, acted as a consultant to various companies, and has served on a number of national and international technical committees and been an Editor, Associate Editor/Guest Editor for five international journals. He has been a keynote/invited speaker and organizer of many conferences and workshops, i.e., WiCom 2006, 2010, IEEE iWAT2010, LAPC2012 and EuCAP2018. He is a member of the UK and Ireland Rep to European Association of Antenna and Propagation (EurAAP), a Fellow of the IET, and Senior Fellow of the HEA. He is currently the Editor-in-Chief of *Wireless Engineering and Technology*, and an Associate Editor of the IEEE Antennas and Wireless Propagation Letters.

QIAN XU (Member, IEEE) received the B.Eng. and M.Eng. degrees from the Department of Electronics and Information, Northwestern Polytechnical University, Xi'an, China, in 2007 and 2010, respectively, and the Ph.D. degree in electrical engineering from the University of Liverpool, U.K, in 2016. He was an RF Engineer in Nanjing, China, in 2011, and an Application Engineer at CST Company, Shanghai, China, in 2012. He is currently an Associate Professor with the College of Electronics and Information Engineering, Nanjing University of Aeronautics and Astronautics, China. His work at the University of Liverpool was sponsored by Rainford EMC Systems Ltd. (now a part of the Microwave Vision Group) and the Centre for Global Eco-Innovation. He has authored the book *Anechoic and Reverberation Chambers: Theory, Design, and Measurements* (Wiley-IEEE, 2019). His research interests include statistical electromagnetics, reverberation chamber, computational electromagnetics, and anechoic chamber.

LYUWEI CHEN received the B.S. degree in electronic sciences and technology from the Jilin Agricultural University, Jilin, China, in 2014, and the M.S. degree in electromagnetic field and electromagnetic wave from Huaqiao University, Xiamen, in 2017. He is currently pursuing the Ph.D. degree in mobile terminal devices antennas with the University of Liverpool, Liverpool, U.K. He was an Antenna and Microwave Engineer with the Shanghai Amphenol Airwave Communication Electronics Company, Ltd., Shanghai, China. His research interests include metamaterials and millimeter-wave array antennas, mobile phone antenna design, the theory of characteristic modes, and MIMO and mm-wave antenna array design for 5G smartphones.

• • •

QIANG HUA received the B.Sc. degree in communication engineering from the University of Liverpool, Liverpool, U.K, in 2016, and the M.Sc. degree in digital signal processing from The University of Manchester, Manchester, U.K, in 2017. He is currently pursuing the Ph.D. degree in base station antennas with the University of Liverpool. His current research focuses on the base station antenna design for 5G in wireless communications.